A Wind Tunnel Study of Ventilation Mechanism over Hypothetical Urban Roughness: the Role of Intermittent Motion Scales

Ziwei Mo and Chun-Ho Liu*
Department of Mechanical Engineering, The University of Hong Kong, Hong Kong

Revised manuscript
Ref. No.: BAE-D-17-01698
submitted
to
Building and Environment
on
February 19, 2018

**Corresponding author address:*
Chun-Ho LIU
Department of Mechanical Engineering
7/F, Haking Wong Building
The University of Hong Kong
Pokfulam Road, Hong Kong, CHINA
Tel: (852) 3917 7901
Fax: (852) 2858 5415
E-mail: liuchunho@graduate.hku.hk

A Wind Tunnel Study of Ventilation Mechanism over Hypothetical Urban Roughness: the Role of Intermittent Motion Scales

Ziwei Mo and Chun-Ho Liu

Department of Mechanical Engineering, The University of Hong Kong, Hong Kong

February 19, 2018

Abstract

Urban morphology is a major factor governing the dynamics in atmospheric surface layers (ASLs) of which our understanding is rather limited. In this paper, wind tunnel experiments are conducted to characterize the flows over different types of urban roughness in attempt to demystify the mechanism of street-level ventilation in isothermal conditions. Hypothetical urban areas are assembled by idealized street canyons using aluminum square tubes (ribs) and plastic LEGO® bricks (cubes). The velocity components are sampled by hot-wire anemometry (HWA) with X-wire probes. The drag coefficient C_d ($= 2u_\tau^2/U_\infty^2$; where u_τ is the friction velocity and U_∞ the freestream wind speed) is used to measure the aerodynamic resistance ($3.588\times10^{-3} \leq C_d \leq 10.799\times10^{-3}$) and parameterize the street-level ventilation of urban areas. The results show that the air exchange rate ACH, as a measure of the aged air removal, is proportional to the root of drag coefficient (ACH $\propto C_d^{1/2}$), implying that rougher urban surfaces favor street-level ventilation. Quadrant analyses illustrate that ejection (Q2) and sweep (Q4) are enhanced by aerodynamic resistance so are the transport processes. Frequency spectra further demonstrate that the dynamics is dominated by large-scale motions ($f\times\delta/u_\tau \leq 10$; where f is the spatial frequency and δ the thickness of turbulent boundary layer) which are more energetic with increasing drag coefficient. The above findings collectively suggest the importance of ASL large scales to street-level ventilation. In addition to promoting ground-level mean wind speed, increasing urban roughness could be a solution to the air quality problems nowadays. (250 words)

Keywords: Air exchange rate ACH, drag coefficient C_d, frequency spectra, quadrant analyses, street-level ventilation and wind tunnel experiments.

1. Introduction

Stagnant air degrades street-level ventilation in urban areas [1]. Massive construction modifies land feature and urban morphology that unavoidably weakens the aged air removal from urban canopy layers (UCLs) [2, 3]. Vast majority eases the problems by promoting ground-level wind speeds which, however, is hard to implement in dense cities nowadays. Advanced understanding of the flows and transport processes in atmospheric surface layers (ASLs) is therefore necessary to enhance street-level ventilation in built environment, improving urban-area air quality [4, 5].

In spite of its importance to urban stakeholders, our understanding of the mechanism for street-level ventilation is rather limited [6, 7]. That is partly why our remedial measures were not as effective as expected so far. This study is therefore conceived, employing turbulent flows over rough surfaces as the theoretical platforms, to elucidate the dynamics over hypothetical urban areas. In particular, we focus on the intermittency and motion scales together with their effects on street-level ventilation. The findings could offer valuable information for architectural design and urban planning in compact, mega cities in the air quality perspective.

Effort has been sought to examine the flows over (hypothetical) urban areas for decades [8, 9, 10]. ASLs develop in response to the presence of building obstacles similar to the conventional rough-wall turbulent boundary layers (TBLs) [5, 11]. Street canyons have been adopted in numerous urban-climate studies which were usually assembled by rib-type roughness elements such as bars or tubes in crossflows [12, 13, 14, 15]. Wind tunnel results over a range of obstacles demonstrated that the height of roughness sublayer (RSL) and inertial sublayer (ISL) was closely affected by the surface roughness [10]. Flows transition from a smoother surface to a rougher one over rib-type roughness elements revealed that the RSL was growing after an abrupt change in aerodynamic resistance before developed into the ISL [16]. The study on the influence of additional small-scale roughness elements on the top of an array of larger two-dimensional (2D) obstacles with different roughness-element-height-to-separation (aspect) ratios (ARs = 1, 2 and 0.5) showed that both the turbulence intensities and the momentum transport were enhanced by the small-scale roughness elements when the ribs were close to each other (ARs = 1 and 2) but not far apart (AR = 0.5) [15]. Hence, AR is not the only factor affecting the transport processes over street canyons that calls for another indicator for geometric configuration.

Apart from rib-type roughness elements, three-dimensional (3D) cube-type roughness elements were employed in wind tunnel experiments to examine urban flows [17]. Vertical profiles of mean wind speed and turbulence were studied over arrays of staggered and aligned cubes with uniform or random height [18]. The RSL was thicker over cubes with random height, arguing that ISL might not exist over extremely rough surfaces. The flows over arrays of cubic roughness elements were characterized by particle image velocimetry (PIV) and/or laser Doppler anemometry (LDA), from which two-point correlation, quadrant analysis and integral length scales were derived [19, 20]. The effect of surface roughness on the aerodynamic parameters by altering the arrangement of cubic obstacles was studied [21]. It was shown that the drag was peaked at certain obstacle density [22, 23]. Although various studies have evaluated the dynamics over different surface types in wind tunnel experiments, our understanding of quantitative ventilation assessments and their mechanism over urban roughness was rather limited.

Real urban morphology is practically too complicated, e.g. frontal area index λ_F (= A_F/A_T; where A_F is the frontal area and A_T the total area) and plan area index λ_P (= A_P/A_T; where A_P is the plan area; Figure 1), are difficult to be measured for air quality analyses so indicators have been formulated to compare street-level ventilation performance quantitatively [24, 25, 26]. Mass transfer coefficients were commonly adopted to measure the transport processes across TBLs that were equally applicable to street-level ventilation performance [27, 28]. Bentham and Britter [29] proposed the use of exchange velocity between the flows in and above the UCL to compare street-level ventilation that was subsequently applied to real inhomogeneous urban geometries as well [30]. Bady et al. [31] compared the reliability of several indicators originally designed for indoor ventilation efficiency, such as purging flow rate (PFR), visitation frequency (VF) and residence time (TP) for outdoor, street-level air quality assessment. The cavity wash-out time, which measures the time scale of mass exchange between street canyons and the ASL aloft, was demonstrated to quantify street-level ventilation performance [32]. Likewise, the concept of city breathability was proposed to analyze pollutant removal from urban areas [33]. Alternatively, from the intermittency point of view, flushing was used to assess the street-level ventilation performance in terms of instantaneous, large-scale turbulence structure prevailing across a street canyon [34]. Urban atmospheric mixing layer height (MLH) was also proposed to calculate the ventilation of an entire city [35]. Apart from VF, Hu and Yoshie [36] simply used the averaged wind speed ratio and the spatially-averaged normalized concentration to assess the street-level ventilation efficiency of a built area. A new design parameter, passage ratio, was then proposed to refine street-level ventilation in urban planning practice. More analogous indoor indicators, such as air change rates per hour and canopy PFR, were proposed to quantify outdoor ventilation capacity [37]. Recently, Lo and Ngan [38] proposed the use of tracer age and age spectrum to measure the ventilation efficiency of a street canyon. The authors also proposed the air exchange rate (ACH), which was subsequent partitioned into mean ACH and turbulent ACH, to diagnose the roof-level aged air (upward) removal from a street canyon [39]. ACH is used in this paper to assess the street-level ventilation performance mainly because of its close relation with the drag coefficient C_d ($= 2u_\tau^2/U_\infty^2$; where u_τ is the friction velocity and U_∞ the freestream wind speed) which is commonly used in wind engineering studies.

Most of the aforementioned indicators compare street-level ventilation in the expense of additional measurements or post-processing of the ventilation variables. Parameterizations, which estimate street-level ventilation utilizing readily available data, are cost-effective measures in particular during design stage. Among various flow variables, Chung and Liu [40] used large-eddy simulation (LES) to showcase the close relation between turbulent ACH and drag coefficient C_d that was subsequently verified by computational fluid dynamics (CFD) results using idealized street canyons of different geometry [41]. Afterward, CFD with the Reynolds-averaged Navier-Stokes (RANS) k-ε turbulence models was performed over various building morphology, such as street canyons of different ARs and buildings of different roof shape, to evaluate the analytical relation [42]. Moreover, in the mechanism perspective, it was revealed that the ventilation over hypothetical urban areas was largely governed by turbulent transport but not mean wind advection in isothermal conditions, arousing our interest looking into ASL intermittency.

A handful of studies have been conducted in the literature to improve our understanding of street-level ventilation mechanism. Using CFD RANS k-ε turbulence models, Baik and Kim [43] suggested that the pollutant removal from street canyons is mainly governed by turbulent processes and the net effect of mean flows is to drive some removed pollutants back into the street canyons. This framework is quite different from the conventional practice using purging to promote street-level ventilation. Concern on scales of motion was raised by Cai et al. [44] in which the limitation of LES was outlined that would under-estimate the transport by large-scale eddies. While aged air removal from ground level is largely governed by intermittency, the concept of plane mixing layer, which is initiated by different flow speeds, was proposed by Letzel et al. [45] to analyze the transport processes over urban areas. Michioka et al. [46], using LES, unveiled that pollutant removal was largely emitted from street canyons by ejection (Q2) of low-momentum fluid. Lately, Liu and Wong [47] suggested that turbulent mixing diluted the ground-level pollutant which was then driven away by prevailing flows, formulating the basic street-level ventilation mechanism. However, these studies only reported CFD results from an analytical approach but lacked of validation using laboratory experiments or field measurements.

In view of the importance of intermittency, this study is conceived in attempt to demystify its role in street-level ventilation mechanism. Because of the close relation between aerodynamic resistance (C_d) and street-level ventilation performance (ACH), we hypothesize that rougher urban surfaces increase aerodynamic resistance that in turn enhance street-level ventilation. In particular, from the motion scales point of view, eddies are tightly influenced by the roughness elements in the near-wall region. How the surface roughness affects the flows and street-level ventilation is another question being addressed. Laboratory wind tunnel experiments are therefore purposely conducted to complement the street-level ventilation mechanism developed by the mathematical modeling studies reviewed above.

In this paper, a series of wind tunnel experiments are carried out to unveil the street-level ventilation mechanism over different (hypothetical) urban morphology. Two types of geometry models are employed, namely ribs as the 2D idealized street canyons (rib-type roughness elements) and LEGO® bricks as the 3D building obstacles (cube-type roughness elements). The wind and turbulence profiles are analyzed to verify the proportionality between ACH and $C_d^{1/2}$ mentioned above. Finally, quadrant analyses and frequency spectra are adopted to elaborate the street-level ventilation mechanism. These findings help advance our fundamental scientific understanding as well as offer handy design information to policy makers and urban planners, effectuating sustainable city design.

2. Theoretical Background

2.1 Air Exchange Rate

ACH is used to quantify the street-level ventilation performance that was defined in Liu et al. [39], as follows

$$\mathrm{ACH} = \int_b w_+\big|_{\mathrm{roof}}\, dx\,. \tag{1}$$

It is integrated only in the streamwise x direction across the width of a unit of street canyon b in this paper because of the homogeneity assumption in the spanwise y direction. The subscript + signifies that only the upward flows (aged air removal) in the wall-normal direction z are considered and the subscript roof denotes the roof-level properties. The (total) ACH is then partitioned into its mean and fluctuating components

$$\mathrm{ACH} = \left\langle \overline{\mathrm{ACH}} \right\rangle + \left\langle \overline{\mathrm{ACH''}} \right\rangle = \int_b \overline{w}_+\big|_{\mathrm{roof}}\, dx + \frac{1}{2} \times \int_b \overline{w''w''}^{1/2}\Big|_{\mathrm{roof}}\, dx\,. \tag{2}$$

Here, overbar $\overline{\phi}$ and angle bracket $\langle \phi \rangle$ denote the temporal and spatial averages, respectively. Double prime represents the deviation from the spatio-temporal average ϕ'' (= $\phi - \langle \overline{\phi} \rangle$). In the last term on the right-hand side of Equation (2), we assume that the roof-level area responsible for upward (removal) and downward (entrainment) flows are equal (because of continuity). The terms $\langle \overline{\mathrm{ACH}} \rangle$ and $\langle \overline{\mathrm{ACH'}} \rangle$ are therefore adopted to measure the ventilation performance driven by mean flows and intermittency, respectively.

Ho et al. [42] demonstrated that practically the street-level ventilation driven by $\langle \overline{\mathrm{ACH}} \rangle$ is small compared with $\langle \overline{\mathrm{ACH'}} \rangle$ for realistic urban areas (less than 30%). It is even smaller for flows over identical, idealized roughness elements. Without loss of generality, we assume ACH $\approx \langle \overline{\mathrm{ACH'}} \rangle$ in the following discussion.

2.2 Linear Relation between ACH'' and $C_d^{1/2}$

Liu et al. [41] employed the momentum conservation and scaling analysis to prove that the fluctuating ACH is proportional to the root of drag coefficient in a dimensionless manner

$$\frac{\left\langle \overline{\mathrm{ACH''}} \right\rangle}{U_\infty b} \propto C_d^{1/2} \tag{3}$$

in details. The mathematics is not repeated here. Equation (3) is therefore a simple parameterization quantifying the effects of urban roughness (in term of drag coefficient) on street-level ventilation performance (in term of ACH). It serves the core of our new parameterization.

3. Methodology

3.1 Wind Tunnel Infrastructure

Experiments are performed in the open-circuit, isothermal wind tunnel in the Department of Mechanical Engineering, The University of Hong Kong. The temperature in the wind-tunnel test section is monitored during experiments to avoid unreasonable fluctuation in thermal conditions. In addition to the flow straightener in-between the settling chamber and the contraction cone, a honeycomb filter is installed afterward to reduce the background turbulence levels ($\leq 5\%$). The flows are driven by a three-phase, electric blower whose power is controlled by a frequency inverter. The wind-tunnel test section, which is made of acrylic, is 6-m long, 0.56-m wide and 0.56-m high. The urban-roughness models are glued on the floor, developing the TBL over a rough surface. Its design wind speed is from 0.5 m sec^{-1} to 15 m sec^{-1}. The freestream wind speed, which is monitored by a pitot tube centered upstream of the test section, is kept in the range of 8 m sec^{-1} $\leq U_\infty \leq$ 11 m sec^{-1}. Details of our wind tunnel infrastructure are available elsewhere [10].

3.2 Urban-Roughness Models

Two types of (hypothetical) urban-rough surfaces are adopted in this study (Table 1). The authors have developed solid experience in the dynamics over idealized rough surfaces. First of all, 2D roughness elements in the form of identical ribs in crossflows are used to formulate the theory (Figure 1a). Aluminum square tubes of size h = 19 mm are placed evenly apart on which the aerodynamic resistance is simply controlled by the separation between the ribs b. Ten configurations of rib-type roughness elements are used to fabricate idealized urban street canyons, whose ARs equal to 1, 1/2, 1/3, 1/4, 1/5, 1/6, 1/8, 1/10, 1/12 and 1/15, are employed, covering the classic regimes of skimming flow, wake interference and isolated roughness [4]. Their drag coefficient is in the range of $4.086\times10^{-3} \leq C_d \leq 10.799\times10^{-3}$.

Afterward, 3D roughness elements in the form of identical cubes are used to verify the newly developed theory. The arrays of 3D cubical roughness elements are built by staggering LEGO® bricks on a LEGO® baseboard (Figure 1b). The size of each piece of LEGO® brick is l (= 16 mm; length) × l (= 16 mm; width) × h (= 11.4 mm; height, including the pins at the top). The separation among the LEGO® bricks is varied in the streamwise x direction, covering h:l, h:2l, h:3l, h:4l, h:5l, h:6l, h:7l, h:8l and h:9l, to control the drag coefficient in the range of $3.588\times10^{-3} \leq C_d \leq 5.458\times10^{-3}$. In addition to the separation apart, the height of roughness elements is increased by mounting double (h:4l-D), triple (h:4l-T) and quadruple (h:4l-Q) layers of LEGO® bricks on the h:4l configuration, extending the drag coefficient to C_d = 7.869×10^{-3}. A total of eleven configurations of cube-type roughness elements are tested.

3.3 Flow Measurements and Data Acquisition

Flows are probed by constant-temperature (CT) hot-wire anemometer (HWA) with a X-wire design to measure streamwise u and vertical w velocity components. The sensing element of the probe consists of a pair of 5-μm (diameter) platinum-plated tungsten wires. By copper electroplating, the active length of the sensing element is 2 mm. The include angle between the two wires is 100º (> 90º) that helps reduce the error due to inadequate yaw response in elevated turbulence intensity in near-wall region [15, 18, 48]. The CT HWA probe is positioned by a mechanical traversing system. It is controlled by the National Instruments (NI) motion control unit whose spatial resolution is 1 mm. The analog CT HWA signal is digitalized by a 24-bit NI data acquisition module (NI 9239; offset error ±0.05% for analog input ±10.52 V) mounted in a NI CompactDAQ chassis (NI cDAQ-9188). The NI units are connected to a digital computer via a local area network (LAN) cable and the data sampling is managed by LabVIEW software. For each test of rough-surface configuration, seven vertical profiles are collected on the wind-tunnel centerplane (y = 0) over a repeating unit of roughness element (Figure 1), covering the top of roughness elements, cavity top, leeward edge and windward edge. A total of 96 sampling points are probed in each vertical profile, ranging from the roughness element height $z = h$ to the wall-normal distance over the TBL z = 350 mm. The sampling time at each point is over 66 sec and the sampling frequency is 2 kHz that are comparable to those employed in literature [15, 18]. Moreover, the sample size (131,072 = 2^{17} data at each sampling point) is sufficient for the repeatability of mean and fluctuating components [49] as well as efficient fast Fourier transform (FFT) on most digital computers. The CT HWA calibration is based on the universal calibration law of the Institute of Sound and Vibration Research (ISVR) [50]. Its readings are compared with those by pitot tube *in-prior* in which the correlation coefficient is up to R^2 = 0.9998.

4. Results and Discussion

In this paper, homogeneity of dynamics is assumed in the spanwise y direction. Hence, x and z denote the streamwise and wall-normal directions, respectively. The wall-normal distance z is measured from the floor of the wind-tunnel test section. The velocities (u, w) are the streamwise and vertical components, respectively. The Reynolds number based on freestream wind speed and TBL thickness Re_∞ (= $U_\infty \delta / \nu$) is in the range of 123,700 ≤ Re_∞ ≤ 264,400 so the molecular viscosity is negligible. Moreover, the Reynolds number based on friction velocity and size of roughness elements Re_τ (= $u_\tau h / \nu$) is well over unity so the flows over the rough surfaces are fully developed (Table 1).

4.1 Rough-Surface Aerodynamic Properties

Dynamics in the TBLs over rough surfaces are characterized by their aerodynamic properties (Table 1). The freestream wind speeds over the rib-type roughness elements (7.97 m sec^{-1} ≤ U_∞ ≤ 9.12 m sec^{-1}) are slower than their cube-type counterparts (9.98 m sec^{-1} ≤ U_∞ ≤ 11.15 m sec^{-1}) that is likely caused by the larger rib size together with the higher aerodynamic resistance. As a result, the TBL thickness over cubes (124×10^{-3} m ≤ δ ≤ 207.8×10^{-3} m) is shallower than that over ribs (205×10^{-3} m ≤ δ ≤ 290×10^{-3} m). On the other hand, the friction velocities u_τ (= $\left|\langle \overline{u''w''} \rangle\right|^{1/2}$) over both types of roughness elements, which are determined based on the roof-level (rather uniform) vertical turbulent momentum flux $u''w''$ [15], are comparable with each other (0.361 m sec^{-1} ≤ u_τ ≤ 0.7 m sec^{-1}). It is thus suggested that surface configuration influences the freestream wind speed across the TBL. Although under-estimate (by 25%) [17] and over-estimate (by 25%) [21] have been observed, it is reasonable to adopt the maximum vertical turbulent momentum flux to determine the friction velocity over rough surfaces [51].

Drag coefficient C_d over different surface configurations are compared in Figure 2. It increases with increasing the separation b between the rib-type roughness elements, arrives the maximum at AR = 1/12 and decreases slightly thereafter for further increasing separation (AR = 1/15). The peaked aerodynamic resistance is attributed to the flow entrainment from the prevailing flow down into the cavity between roughness elements and the subsequent flow impingement on their windward side. A plateau of drag coefficient is clearly depicted in 1/5 ≤ h/b ≤1/15 in which the variation is mild (≈ 10%). It is caused by the flow-impingement dominated aerodynamic resistance so the drag coefficient is likely a function of the size of roughness elements h rather than their separation apart b [40, 52]. A similar feature is observed for the flows over staggered cube-type roughness elements. The drag coefficient increases with increasing separation between the cubes, reaches the peak in the case h:4l, and decreases thereafter. It almost flats out when the separation is larger than 4l units that is in line with the aforementioned flow-impingement dominated aerodynamic resistance over rib-type roughness elements. Additional layers of LEGO® bricks on roughness elements (*h*:4*l*-D, *h*:4*l*-T and *h*:4*l*-Q) increase the drag coefficient that is attributed to the larger size of roughness elements together with their blockage variability, promoting flow impingement.

The parameters measuring aerodynamic resistance, including displacement height d and roughness length z_0, are determined by the best fit of the measured mean wind speed to the conventional logarithmic law of the wall (log-law) [15, 16, 18]. Displacement height d is used to offset the blockage of roughness elements for mean-wind profile regression that is interpreted as the force center on the windward faces of roughness elements [53]. Apparently, the entrainment is deeper for multi-layer cubes (likely because of the staggered arrangement), so the displacement height descends to the lower half of ribs and slightly over the mid-level of single-layer cubes. These ranges of displacement height, which are $0.208 \leq d/h \leq 0.713$ for ribs and $0.095 \leq d/h \leq 0.6$ for cubes, are also comparable with those available in literature [21, 32]. Whereas, it does not show any notable relation with the drag coefficient (Table 1). Roughness length scale z_0 is another parameter commonly used to measure surface roughness. Its trend over rib-type roughness elements is generally consistent with that of the drag coefficient (Figure 2a). Whereas, the roughness length scale z_0 shows mild differences from the drag coefficient C_d for the flows over cube-type roughness elements (Figure 2b). The differences are found after additional layers of LEGO® brick are introduced. Comparing with the case *h*:4*l*, slightly increasing the size of roughness elements indeed reduces the roughness length scale of the case *h*:4*l*-D by 10%. Additional LEGO® brick layers, say cases *h*:4*l*-T and *h*:4*l*-Q, pick up the roughness length scale alike the drag coefficient. Flow impingement is enhanced for flows over roughness elements of non-uniform height that results in substantial vertical flows. Hence, the flows are no longer uniform in the streamwise direction x that in turn weakens the applicability of the conventional log-law so does the representation of z_0 and d for aerodynamic resistance. Nonetheless, the discrepancy is small and the current wind-tunnel measurements are in line with those in literature such that C_d increases with increasing z_0 in principle [54]. When the separation of cube-type roughness elements is longer than 6*l*, further increasing the separation suppresses the roughness length scale instead. Under this circumstance, the use of roughness length scale z_0 to measure the aerodynamic resistance over rough surfaces should be interpreted cautiously.

In the current isothermal conditions, the TBL thickness δ is largely governed by the geometry of the roughness elements. It is determined by the wall-normal distance where the spatio-temporal wind speed converges to 99% of the freestream wind speed $\left\langle \overline{u} \right\rangle \Big|_{z=\delta} = 0.99U_{\infty}$. The values of dimensionless TBL thickness δ, which are measured in terms of roughness-element size, are comparable for the two types of roughness elements ($7h \le \delta \le 16h$). This range of TBL thickness over homogeneous roughness is also similar to that available in literature, say ribs [16], cubes [18] as well as LEGO® bricks [21]. Additional LEGO® brick layers in fact reduce the dimensionless TBL thickness because the size of those cube-type roughness elements is increased. In fact the (dimensional) TBL thickness δ is increased by 20% (h:4l-D) to almost 40% (h:4l-Q). As such, the size of roughness elements is unlikely a factor governing TBL thickness.

4.2 Flows and Turbulence

Dimensionless mean wind speeds $\left\langle \overline{u} \right\rangle / U_{\infty}$ over different types of roughness elements exhibit similar characteristics that converge gradually toward the TBL top (Figure 3a). A mild difference is observed in the near-wall region close to the roughness elements, signifying the range of influence of aerodynamic resistance on the mean-wind profiles. Section 4.1 discusses the effect of surface roughness that could act on the freestream wind speed U_{∞} across the TBL reaching the top in the wind tunnel experiments. While the freestream wind speed is a suitable characteristic velocity scale, the surface roughness in fact modifies the velocity gradient so does the turbulent transport processes in the near-wall region.

The profiles of dimensionless streamwise fluctuating velocity $\left\langle \overline{u''u''} \right\rangle^{1/2} / u_{\tau}$ decrease almost linearly with increasing wall-normal distance (Figure 3b). Their maximum values are similar ($2.2u_{\tau} \le \left\langle \overline{u''u''} \right\rangle^{1/2} \le 2.6u_{\tau}$) right over the roughness elements, suggesting their mechanically generated nature and the relation with the friction velocity. The profiles of dimensionless vertical fluctuating velocity $\left\langle \overline{w''w''} \right\rangle^{1/2} / u_{\tau}$ also decrease with increasing wall-normal distance (Figure 3c). Whereas, different from their streamwise counterparts, broad maxima ($u_{\tau} \le \left\langle \overline{w''w''} \right\rangle^{1/2} \le 1.2u_{\tau}$) are developed within $0.1\delta \le (z - h) \le 0.4\delta$. Besides, in the vicinity to the rough surfaces for $(z - h) \le 0.1\delta$, the vertical fluctuating velocities right over the roughness elements show diversified behaviors such that they vary in the range $u_\tau \leq \langle \overline{w''w''} \rangle^{1/2} \leq 1.5u_\tau$. The variation is over 30% that could be due to the RSL effects of individual roughness elements. Both streamwise and vertical fluctuating velocities exhibit sparse data toward the TBL top where their levels are less than $0.5u_\tau$. Therefore, the friction velocity is no longer an appropriate scale to the flows in the upper TBL. Momentum flux governs the transport processes, reflecting the correlation between the streamwise and vertical velocity components. These two velocity components are tightly affect each other in the lower TBL (momentum flux is close to unity) but decouple near the TBL top (Figure 3d). The peaks of the dimensionless momentum flux $\langle \overline{u''w''} \rangle / u_\tau^2$ are elevated in the range of $0.05\delta \leq (z - h) \leq 0.2\delta$, developing the constant-flux surface layer in most rough-surface flows. Apparently, the constant-flux layers over rib-type (cube-type) roughness elements are thicker (thinner) elevating at a higher level (in the near-wall region). The profiles of momentum flux over the two types of roughness elements show slightly different behaviors. The dimensionless momentum flux data collected based on cube-type roughness elements collapse onto a single curve while those based on rib-type are sparse. Nevertheless, they are linearly decreasing similar to those of theoretical open-channel flows. The dimensionless momentum fluxes in the TBL core over rib-type roughness elements are generally larger than their cube-type counterparts. This dissimilarity could be attributed to the 2D flow nature around and over rib-type roughness elements together with their larger size so the correlation between streamwise and vertical velocities persists in the mid-level TBL.

The effect of surface roughness on mean flows are more notable when the dimensionless mean wind speed, which is normalized by the friction velocity u_τ instead of the freestream mean wind speed U_∞, is expressed in semi-logarithmic scale. It is well known fact that the conventional log-law $\langle \overline{u} \rangle / u_\tau = 1/\kappa \times \ln[(z-d)/z_0]$, where κ (= 0.4) is the von Kármán constant, is applicable over rough surfaces. Other values of κ (0.38 to 0.41) have been reported elsewhere [17, 21, 55]. Nonetheless, the constant does not change too much the trend of d and z_0 in response to aerodynamic resistance. The log-law is clearly exhibited in the flows over both rib-type and cube-type roughness elements (Figure 3). The ISL height, within which the log-law applies, is determined at the wall-normal distance z where the dimensionless wind-speed gradient $\kappa z / u_\tau \times d\langle \overline{u} \rangle / dz$ is outside 1 ± 0.05. The ISL is clearly displayed though its thickness is shallow (as reflected by the thin constant-flux layers). The profiles of dimensionless mean wind speed generally shift downward with increasing roughness length scale z_0 over rougher surfaces. The limitation of roughness length scale z_0 measuring aerodynamic resistance is discussed in Section 4.1. In this paper, the rib-type roughness elements are generally rougher than the cube-type that is a result of the 2D flows and larger roughness element size.

4.3 Street-Level Ventilation and Drag Coefficient

Parameterization of street-level ventilation in terms of ACH was suggested by Ho et al. [42] in which the dimensionless turbulent ACH is proportional to the root of drag coefficient (Equation 3). This formulation is tested again in this paper using both rib- and cube-type roughness elements that shows a reasonable behavior of linearity (correlation coefficient R^2 = 0.68; Figure 5). For the rib-type roughness elements alone, R^2 is equal to 0.75 in which a notable discrepancy is found in the flows with a larger drag coefficient ($C_d \approx 0.01$). In this flow regime, the aerodynamic resistance converges that is dominated by flow impingement on the windward walls of roughness elements. Under this circumstance, $\langle \overline{\mathrm{ACH''}} \rangle$ levels off so the relatively contribution from $\langle \overline{\mathrm{ACH}} \rangle$ increases. The drag coefficient is however unable to parameterize $\langle \overline{\mathrm{ACH}} \rangle$, resulting in the uncertain ACH parameterization in the isolated roughness regime. For the ACH over cube-type roughness elements alone, the parameterization is improved compared with that for rib-type roughness elements alone because R^2 increases from 0.75 to 0.86. The slope and y-intercept of the aforementioned regressions show slight differences which are likely attributed to the different experimental conditions such as freestream wind speed, background turbulence intensity and TBL thickness. Nonetheless, the reasonably tight correlation based on the two types of roughness elements suggests the feasibility of developing an ACH parameterization in the engineering perspective. Hence, a parameterization is developed to help interpret the ventilation mechanism, which focuses on the dynamics, in the next section.

4.4 Ventilation Mechanism

Because intermittency dominates the dynamics in street-level ventilation, quadrant analyses and frequency spectra are used to elucidate the mechanism in particular the turbulent transport processes. As the (linear) proportionality between (the root of) drag coefficient and

ACH is derived previously, the following discussion focuses on the aerodynamic resistance and the flow intermittency instead of using street-level ventilation indicators.

4.4.1 Quadrant Analyses

Quadrant analyses are employed to demystify the intermittent turbulent transport processes over rough surfaces. Based on the instantaneous fluctuating velocity components, events of momentum flux are categorized into four quadrants (Table 2) which are compared to examine their contributions to the turbulent transport processes of vertical momentum flux $u''w''$ and the associated ventilation mechanism (because of the Reynolds analogy). Moreover, we adopt the joint probability density function (JPDF) $P(u'', w'')$ and the covariance integrand $u''w''P(u'', w'')$

$$\left\langle \overline{u''w''} \right\rangle = \int_{-\infty}^{+\infty} u''w''P\left(u'', w''\right) du''dw'' \tag{4}$$

suggested by Wallace [56] to examine the dynamics. The JPDF and covariance integrand measure the frequency of occurrence and the strength of individual events, respectively. The JPDF signifies the likely occurrence of a quadrant event in terms of the fluctuating velocity components u'' and w''. It is calculated according to the ratio of the occurrences of individual quadrants to the total number of data samples. Figure 6 shows clearly that the JPDF is peaked at small fluctuating velocities over smoother surfaces. It spreads out in the directions of ejection Q2 and sweep Q4 with increasing aerodynamic resistance. The elongated shaded contours imply that the occurrence of outward interaction Q1 and inward interaction Q3 are suppressed over rougher surfaces (Figure 6).

The covariance integrand, on the other hand, includes the strength of the dynamics to account for the influence on turbulent momentum transport. Flows over the rib- and cube-type roughness elements exhibit more frequent events of ejection Q2 and sweep Q4 than outward interaction Q1 and inward interaction Q3 as reflected from the contour lines of covariance integrand (Figure 6). Although all the four events govern momentum transport, from the street-level ventilation point of view, higher values of covariance integrand Q2 and Q4 unveil that fresh air entrainment ($w'' \leq 0$) and aged air removal ($w'' \geq 0$) are driven by decelerating ($u'' \leq 0$) and accelerating ($u'' \geq 0$) air masses, respectively. This observation is in line with that calculated previously by LES [47]. The transport processes over smoother surfaces are more homogeneous so the covariance integrand distributes more uniformly among the four quadrants over smoother surfaces (AR=1 and h/l). A wider range of fluctuating velocities relative to friction velocity u_i''/u_τ is observed for flows over AR=1/12 and h:4l-Q (rougher) compared with AR=1 and h:l (smoother) surfaces that agrees with the laboratory measurements over a single street canyon [57]. Extreme events of ejection Q2 and sweep Q4, which are indicated by the negative contours, occur more frequently over rougher surfaces. It is likely attributed to the accelerating (decelerating) flow entrainment (removal). Moreover, the occurrence of outward interaction Q1 and inward interaction Q3, which are indicated by the positive contours, is weakened with increasing aerodynamic resistance. It is thus demonstrated that rougher surfaces strengthen extreme events Q2 and Q4. Subsequently, ACH is enhanced, resulting in the more efficient street-level ventilation over rougher urban areas where stronger updraft (decelerating air masses) and downdraft (accelerating air masses) are more favorable.

4.4.2 Frequency Spectra

Finally, frequency spectra are performed to examine the turbulence motion scales right over the roughness elements at $z = h$ [58]. FFT is used to convert the time traces of fluctuating velocities at the center of street canyons from time domain to frequency domain [59]. Taylor hypothesis is used to convert the temporal signal to spatial signal utilizing the data collected from a stationary CT HWA sampling probe in the streamwise x direction. The energy spectra cover almost five orders of magnitude of spatial/temporal scales in which a similar pattern of frequency spectra is found for the flows over rib-type and cube-type roughness elements (Figure 7). They decrease sharply when the dimensionless frequency $f\times\delta/u_\tau > 1$ for the streamwise u'' and $f\times\delta/u_\tau > 10$ for the vertical w'' fluctuating velocities. The conventional inertial subrange with a -5/3 slope is also clearly exhibited, illustrating the energy cascade of rough-surface flows in isothermal conditions. Another observation is that the peaked energy spectra of u'' are higher than those of w'' over an order of magnitude. Besides, the energy spectra of fluctuating streamwise and vertical velocities are of comparable magnitude for $f\times\delta/u_\tau > 100$, depicting the isotropy of small-scale motions as well as the sufficient sampling frequency adopted in this study. It is noteworthy that a mild difference in energy spectra over surfaces of different roughness is observed. In the low-frequency fraction, the energy spectra over rib-type roughness elements are generally higher than their cube-type counterparts (by two to three times as shown in the inserted figures). The effect of surface roughness on the energy spectra is less obvious for flows over the rib-type roughness elements. While the magnitude of energy spectra is trough at AR=1 ($C_d = 4.086\times10^{-3}$), it is peaked at AR=1/6 ($C_d = 9.875\times10^{-3}$) instead of AR=1/12 ($C_d = 10.799\times10^{-3}$) that is not consistent with the trend of motion scales in response to drag coefficient. This discrepancy is likely attributed to the small difference in drag coefficient (9.357%) between the cases AR=1/6 and AR=1/12. On the other hand, the effect of drag coefficient on the energy spectra of flows over cube-type roughness elements is more notable, the energy spectra are least at *h*:*l* ($C_d = 3.588\times10^{-3}$), followed by *h*:6*l* ($C_d = 5.098\times10^{-3}$) and peaked at *h*:4*l*-Q ($C_d = 7.869\times10^{-3}$). This finding also concurs the importance of extreme events in street-level ventilation discussed by quadrant analyses in Section 4.4.1 above, demonstrating the importance of large-scale motions in street-level ventilation. Hence, the drag over rough surfaces could enhance large-scale motions so does the street-level ventilation performance. In view of the almost constant dimensionless fluctuating velocities $\left\langle \overline{u_i''u_i''} \right\rangle / u_\tau^2$ over different rough surfaces, consequence of modifying the large scales is reflected in the small scales as well. More energetic small-scale motions are observed over smoother surfaces, which, however, do not help much street-level ventilation because of the much weaker motion scales as shown in the covariance integrand Equation (4).

5. Conclusions

A series of wind tunnel experiments are conducted in this study to characterize the street-level ventilation over hypothetical urban areas in isothermal conditions. Rib- and cube-type roughness elements are adopted fabricating the hypothetical urban-rough surfaces in order to contrast the dynamics over different configurations of building morphology. Vertical profiles of streamwise $\left\langle \overline{u''u''} \right\rangle^{1/2}$ and vertical $\left\langle \overline{w''w''} \right\rangle^{1/2}$ fluctuating velocities together with momentum flux $\left\langle \overline{u''w''} \right\rangle$ collectively show that near-wall flows and transport processes are tightly affected by the aerodynamic resistance induced by the roughness elements. Sensitivity tests using both rib- and cube-type roughness elements consistently demonstrate that the linear proportionality $\left\langle \overline{\mathrm{ACH''}} \right\rangle / U_\infty b \propto C_d^{1/2}$ is equally applicable to 2D and 3D building morphology that could be a handy parameterization to street-level ventilation in practice. In view of the dominated intermittent transport processes, quadrant analyses and frequency spectra are conducted to demystify the ventilation mechanism. Similar to their smooth-wall counterparts, ejection Q2 and sweep Q4 are the major transport processes. Moreover, the covariance integrand of Q2 and Q4 (Q1 and Q3) is enhanced (is suppressed) with increasing (decreasing) drag coefficient that partly explains the more favorable street-level ventilation over rougher urban surfaces and the importance of strong, extreme events to the improvement of urban air quality. Frequency spectra generally show that increasing (decreasing) aerodynamic resistance strengthens the large-scale (small-scale) motions. Hence, large-scale intermittent motions, which mainly exist in the background atmospheric flows, play key roles in street-level ventilation mechanism. These findings shed some light on the ventilation mechanism, providing valuable information to policy makers and practitioners.

Acknowledgements

The authors would like to thank the editor and the anonymous reviewers for their invaluable suggestion to improve the manuscript. This study is supported by the General Research Fund (GRF) 17205314 of the Hong Kong Research Grants Council (RGC).

References

[1] B.R. Gurjar, T.M. Butler, M.G. Lawrence, J. Lelieveld, Evaluation of emissions and air quality in megacities, Atmos. Environ. 42 (2008) 1593-1606.

[2] E. Ng, Policies and technical guidelines for urban planning of high-density cities – air ventilation assessment (AVA) of Hong Kong, Build. Environ. 44 (2009) 1478-1488.

[3] K.K. Leung, C.-H. Liu, C.C.C. Wong, J.C.Y. Lo, G.C.T. Ng, On the study of ventilation and pollutant removal over idealized two-dimensional urban street canyons, Build. Simul. 5 (2012) 359-369.

[4] T.R. Oke, Street design and urban canopy layer climate, Energ. Buildings 11 (1988) 103-113.

[5] J. Jiménez, Turbulent flows over rough walls, Annu. Rev. Fluid. Mech. 36 (2004) 173-196.

[6] C. Yuan, E. Ng, Building porosity for better urban ventilation in high-density cities – a computational parametric study. Build. Environ. 50 (2012) 176-189.

[7] W. Wang, E. Ng, Air ventilation assessment under unstable atmospheric stratification - a comparative study for Hong Kong. Build. Environ. 130 (2018) 1-13.

[8] R.E. Britter, S.R. Hanna, Flow and dispersion in urban areas, Annu. Rev. Fluid. Mech. 35 (2003) 469-496.

[9] M. Carpentieri, A.G. Robins, Influence of urban morphology on air flow over building arrays, J. Wind. Eng. Ind. Aerodyn. 145 (2015) 61-74.

[10] J.F. Barlow, Progress in observing and modelling the urban boundary layer, Urban Climate 10 (2010) 216-240.

[11] S.B. Pope, Turbulent Flows, Cambridge University Press, Cambridge, U.K (2000).

[12] R. N. Meroney, M. Pavageau, S. Rafailidis, M. Schatzmann, Study of line source characteristics for 2-D physical modelling of pollutant dispersion in street canyons, J. Wind Eng. Ind. Aerodyn. 62 (1) (1996) 37-56.

[13] M. Pavageau, M. Schatzmann, Wind tunnel measurements of concentration fluctuations in an urban street canyon, Atmos. Environ. 33 (1999) 3961-3971.

[14] Y.K. Ho, C.-H. Liu, A wind tunnel study of flows over idealised urban surfaces with roughness sublayer corrections, Theor. Appl. Climatol. 130 (2017) 305-320.

[15] P. Salizzoni, L. Soulhac, P. Mejean, R.J. Perkins, Influence of a two-scale surface roughness on a neutral turbulent boundary layer, Boundary-Layer Meteorol. 127 (2008) 97-110.

[16] H. Cheng, H. I.P. Castro, Near-wall flow development after a step change in surface roughness, Boundary-Layer Meteorol. 105 (3) (2002) 411-432.

[17] H. Cheng, P. Hayden, A.G. Robins, I.P. Castro, Flow over cube arrays of different packing densities, J. Wind. Eng. Ind. Aerodyn. 95 (2007) 715-740.

[18] H. Cheng, I.P. Castro, Near wall flow over urban-like roughness, Boundary-Layer Meteorol. 104 (2002) 229-259.

[19] I. P. Castro, H. Cheng, R. Reynolds, Turbulence over urban-type roughness: deductions from wind-tunnel measurements, Boundary-Layer Meteorol. 118 (1) (2006) 109-131.

[20] R. T. Reynolds, I. P. Castro, Measurements in an urban-type boundary layer, Exp. Fluids 45 (1) (2008), 141-156.

[21] M. Placidi, B. Ganapathisubramani, Effects of frontal and plan solidities on aerodynamic parameters and the roughness sublayer in turbulent boundary layers, J. Fluid Mech. 782 (2015) 541-566.

[22] S.A. Zaki, A. Hagishima, J. Tanimoto, N. Ikegaya, Aerodynamic parameters of urban building arrays with random geometries, Boundary-Layer Meteorol. 138 (2011) 99-120.

[23] A.F. Mohammad, S.A. Zaki, A. Hagishima, M.S.M. Ali, Determination of aerodynamic parameters of urban surfaces: methods and results revisited, Theor. Appl. Climatol. (2015) 122, 635-649.

[24] N. Antoniou, H. Montazeri, H. Wigo, M.K.A. Neophytou, B. Blocken, M. Sandberg, CFD and wind-tunnel analysis of outdoor ventilation in a real compact heterogeneous urban area: evaluation using "air delay", Build. Environ. 126 (2017) 355-372.

[25] A. Ricci, M. Burlando, A. Freda, M.P. Repetto, Wind tunnel measurements of the urban boundary layer development over a historical district in Italy. Build. Environ. 111 (2017) 192-206.

[26] L. Chen, J. Hang, M. Sandberg, L. Claesson, S. Di Sabatino, H. Wigo, The impacts of building height variations and building packing densities on flow adjustment and city breathability in idealized urban models, Build. Environ. 118 (2017) 344-361.

[27] F. Pascheke, J.F. Barlow, A.G. Robins, Wind-tunnel modelling of dispersion from a scalar area source in urban-like roughness, Boundary-Layer Meteorol. 126 (2008) 103–124.

[28] N. Ikegaya, A. Hagishima, J. Tanimoto, Y. Tanaka, K.I. Narita, S.A. Zaki, Geometric dependence of the scalar transfer efficiency over rough surfaces, Boundary-Layer Meteorol.143 (2012) 357–377.

[29] T. Bentham, R. Britter, Spatially averaged flow within obstacle arrays, Atmos. Environ. 37 (2003) 2037-2043.

[30] I. Panagiotou, M.K.A. Neophytou, D. Hamlyn, D. R.E. Britter, City breathability as quantified by the exchange velocity and its spatial variation in real inhomogeneous urban geometries: an example from central London urban area, Sci. Total Environ. 442 (2013) 466-477.

[31] M. Bady, S. Kato, H. Huang, Towards the application of indoor ventilation efficiency indices to evaluate the air quality of urban areas, Build. Environ. 43 (2008) 1991-2004.

[32] P. Salizzoni, L. Soulhac, P. Mejean, Street canyon ventilation and atmospheric turbulence, Atmos. Environ. 43 (2009) 5056–5067.

[33] R. Buccolieri, M. Sandberg, S. Di Sabatino, City breathability and its link to pollutant concentration distribution within urban-like geometries, Atmos. Environ. 44 (2010) 1894-1903.

[34] H. Takimoto, A. Sato, J.F. Barlow, R. Moriwaki, A. Inagaki, S. Onomura, M. Kanda, Particle image velocimetry measurements of turbulent flow within outdoor and indoor urban scale models and flushing motions in urban canopy layers, Boundary-Layer Meteorol. 140 (2011) 295–314.

[35] Q. Deng, G. He, C. Lu, W. Liu, Urban ventilation – a new concept and lumped model, Int. J. Vent. 11 (2012) 131-140.

[36] T. Hu, R. Yoshie, Indices to evaluate ventilation efficiency in newly-built urban area at pedestrian level, J. Wind Eng. Ind. Aerodyn. 112 (2013) 39-51.

[37] M. Lin, J. Hang, Y. Li, Z. Luo, M. Sandberg, Quantitative ventilation assessments of idealized urban canopy layers with various urban layouts and the same building packing density, Build. Environ. 79 (2014) 152-167.

[38] K.W. Lo, K. Ngan, Characterising the pollutant ventilation characteristics of street canyons using the tracer age and age spectrum, Atmos. Environ. 122 (2015) 611-621.

[39] C.-H. Liu, D.Y.C. Leung, M.C. Barth, On the prediction of air and pollutant exchange rates in street canyons of different aspect ratios using large-eddy simulation, Atmos. Environ. 39 (9) (2005) 1567-1574.

[40] T.N.H. Chung, C.-H. Liu, On the mechanism of air pollutant removal in two-dimensional idealized street canyons: a large-eddy simulation approach, Boundary-Layer Meteorol. 148 (2013) 241-253.

[41] C.-H. Liu, C.T. Ng, C.C.C. Wong, A theory of ventilation estimate over hypothetical urban areas, J. Hazard. Mater. 296 (2015) 9-16.

[42] Y.K. Ho, C.-H. Liu, M.S. Wong, Preliminary study of the parameterisation of street-level ventilation in idealised two-dimensional simulations, Build. Environ. 89 (2015) 345-355.

[43] J.J. Baik, J.J. Kim, On the escape of pollutants from urban street canyons, Atmos. Environ. 36 (2002) 527-536.

[44] X. Cai, J.F. Barlow, S.E. Belcher, Dispersion and transfer of passive scalars in and above street canyons - large-eddy simulations, Atmos. Environ. 42 (2008) 5885-5895.

[45] M.O. Letzel, M. Krane, S. Raasch, High resolution urban large-eddy simulation studies from street canyon to neighbourhood scale, Atmos. Environ. 42 (2008) 8770-8784.

[46] T. Michioka, A. Sato, H. Takimoto, M. Kanda, Large-eddy simulation for the mechanism of pollutant removal from a two-dimensional street canyon, Boundary-Layer Meteorol. 138 (2011) 195-213.

[47] C.-H. Liu, C.C.C. Wong, On the pollutant removal, dispersion, and entrainment over two-dimensional idealized street canyons, Atmos. Res. 135-136 (2014) 128-142.

[48] A.E. Perry, K.L. Lim, S.M. Henbest, An experimental study of the turbulence structure in smooth- and rough-wall boundary layers, J. Fluid Mech. 177 (1987) 437-466.

[49] A. Robins, Wind tunnel dispersion modelling some recent and not so recent achievements, J. Wind. Eng. Ind. Aerodyn. 91 (2003) 1777–1790

[50] H. Bruun, Interpretation of a hot wire signal using a universal calibration law, J. Phys. E. Sci. Instrum. 4 (1971) 225.

[51] C. Manes, D. Poggi, L. Ridolfi, Turbulent boundary layers over permeable walls: scaling and near-wall structure, J. Fluid Mech. 687 (2011) 141-170.

[52] C.-H. Liu, T.N.H. Chung, Forced convective heat transfer over ribs at various separation, Int. J. Heat Mass Transfer 55 (2012) 5111-5119.

[53] P. Jackson, On the displacement height in the logarithmic velocity profile, J. Fluid Mech. 111 (1981) 15-25.

[54] A. Hagishima, J. Tanimoto, K. Nagayama, S. Meno, Aerodynamic parameters of regular arrays of rectangular blocks with various geometries, Boundary-Layer Meteorol. 132 (2009) 315-337.

[55] M. Acharya, J. Bornstein, M.P. Escudier, Turbulent boundary layers on rough surfaces, Exp. Fluids 4 (1986) 33–47.

[56] J.M. Wallace, Quadrant analysis in turbulence research: history and evolution, Annu. Rev. Fluid Mech. 48 (2016) 131-158.

[57] M. Immer, J. Allegrini, J. Carmeliet, Time-resolved and time-averaged stereo-PIV measurements of a unit-ratio cavity, Exp. Fluids 57 (2016) 101-118.

[58] L.A. El-Gabry, D.R. Thurman, P.E. Poinsatte, Procedure for determining turbulence length scales using hotwire anemometry, (2014).

[59] B.D. Storey, Computing Fourier series and power spectrum with Matlab, TEX paper (2002).

Table 1. Parameters of the wind tunnel experiments.

Rough surfaces	U_∞ (m sec^{-1})	u_τ (m sec^{-1})	u_τ/U_∞	C_d ($\times10^{-3}$)	δ ($\times10^{-3}$ m)	h ($\times10^{-3}$ m)	δ/h	Re_∞	Re_τ	d/h	z_0/h
Rib-type roughness elements											
AR = 1/1	7.99	0.361	0.045	4.086	205	19	11	163,700	7,400	0.317	0.002
AR = 1/2	7.97	0.453	0.057	6.457	230	19	12	183,300	10,400	0.363	0.023
AR = 1/3	8.36	0.515	0.062	7.599	233	19	12	194,700	12,000	0.311	0.033
AR = 1/4	8.45	0.556	0.066	8.667	268	19	14	226,400	14,900	0.371	0.043
AR = 1/5	8.53	0.591	0.069	9.607	270	19	14	230,300	16,000	0.325	0.055
AR = 1/6	8.50	0.597	0.07	9.875	280	19	15	238,000	16,700	0.322	0.052
AR = 1/8	8.40	0.597	0.071	10.114	280	19	15	235,100	16,700	0.208	0.055
AR = 1/10	9.08	0.645	0.071	10.073	290	19	15	263,400	18,700	0.439	0.042
AR = 1/12	9.12	0.67	0.073	10.799	290	19	15	264,400	19,400	0.713	0.045
AR = 1/15	9.04	0.641	0.071	10.063	278	19	15	251,200	17,800	0.613	0.039
Cube-type roughness elements											
h:l	9.98	0.423	0.042	3.588	124	9.6	13	123,700	5,200	0.54	0.002
h:2l	10.85	0.530	0.049	4.766	154	9.6	16	167,100	8,200	0.6	0.008
h:3l	10.83	0.536	0.049	4.897	154	9.6	16	166,800	8,300	0.554	0.01
h:4l	10.79	0.564	0.052	5.458	154	9.6	16	166,200	8,700	0.585	0.013
h:5l	10.59	0.542	0.051	5.243	149	9.6	16	157,800	8,100	0.564	0.011
h:6l	10.61	0.536	0.05	5.098	154	9.6	16	163,400	8,300	0.552	0.011
h:7l	10.64	0.532	0.05	4.998	149	9.6	16	158,500	7,900	0.521	0.009
h:9l	10.73	0.512	0.048	4.543	144	9.6	15	154, 600	7,400	0.503	0.006
h:4l-D	10.77	0.603	0.056	6.27	179	19.2	9	192,300	10,800	0.3	0.012
h:4l-T	11.06	0.661	0.06	7.144	203	24.0	8	224,700	13,400	0.177	0.013
h:4l-Q	11.15	0.7	0.063	7.869	208	28.8	7	231,800	14,500	0.095	0.014

Table 2. Quadrants of vertical turbulent momentum flux $u''w''$.

Quadrants	Events	u''	w''
Q1	Outward interaction	+	+
Q2	Ejection	-	+
Q3	Inward interaction	-	-
Q4	Sweep	+	-

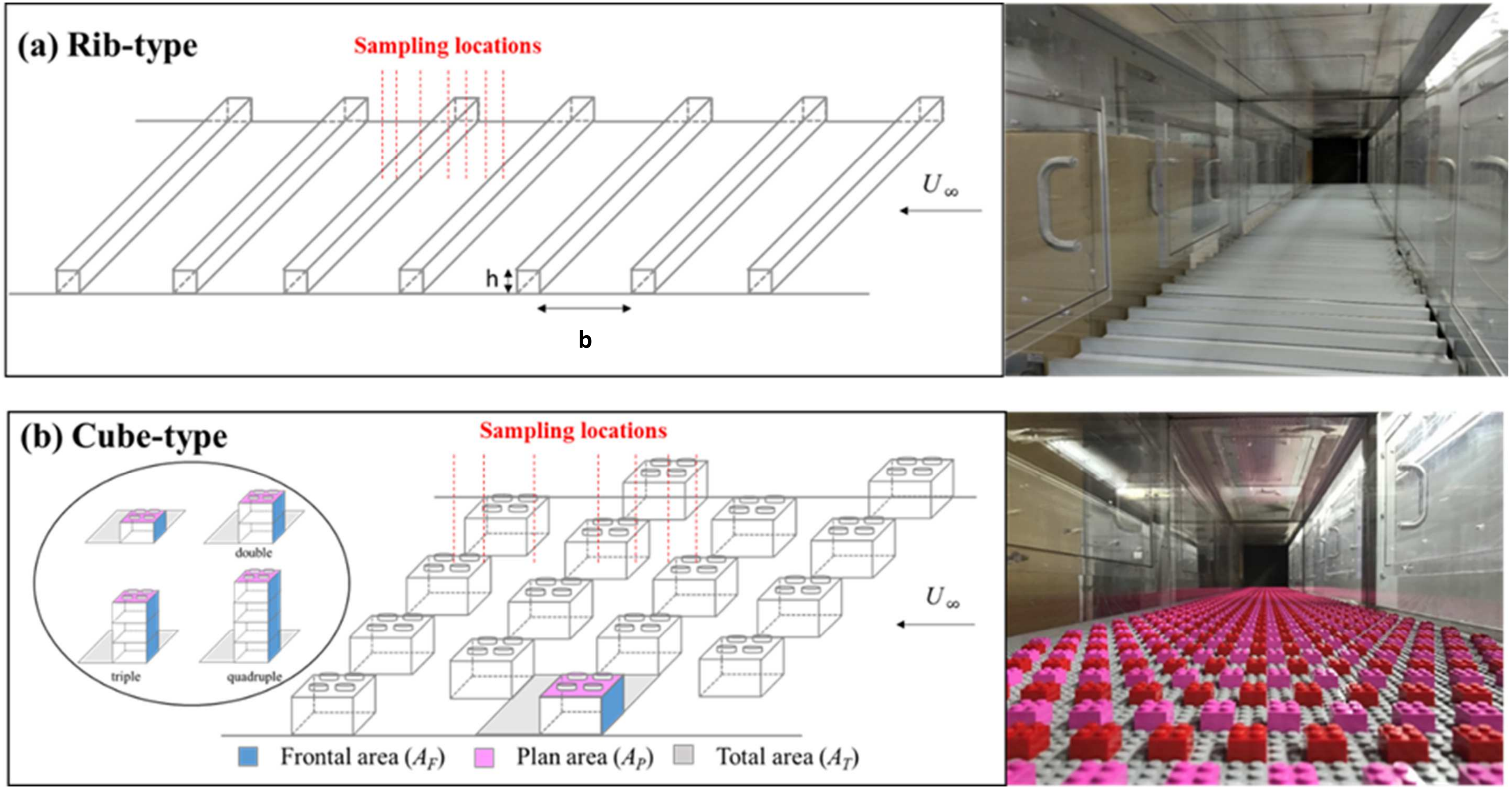

Figure 1. (a) Rib- and (b) cube-type roughness elements in the wind tunnel experiments.

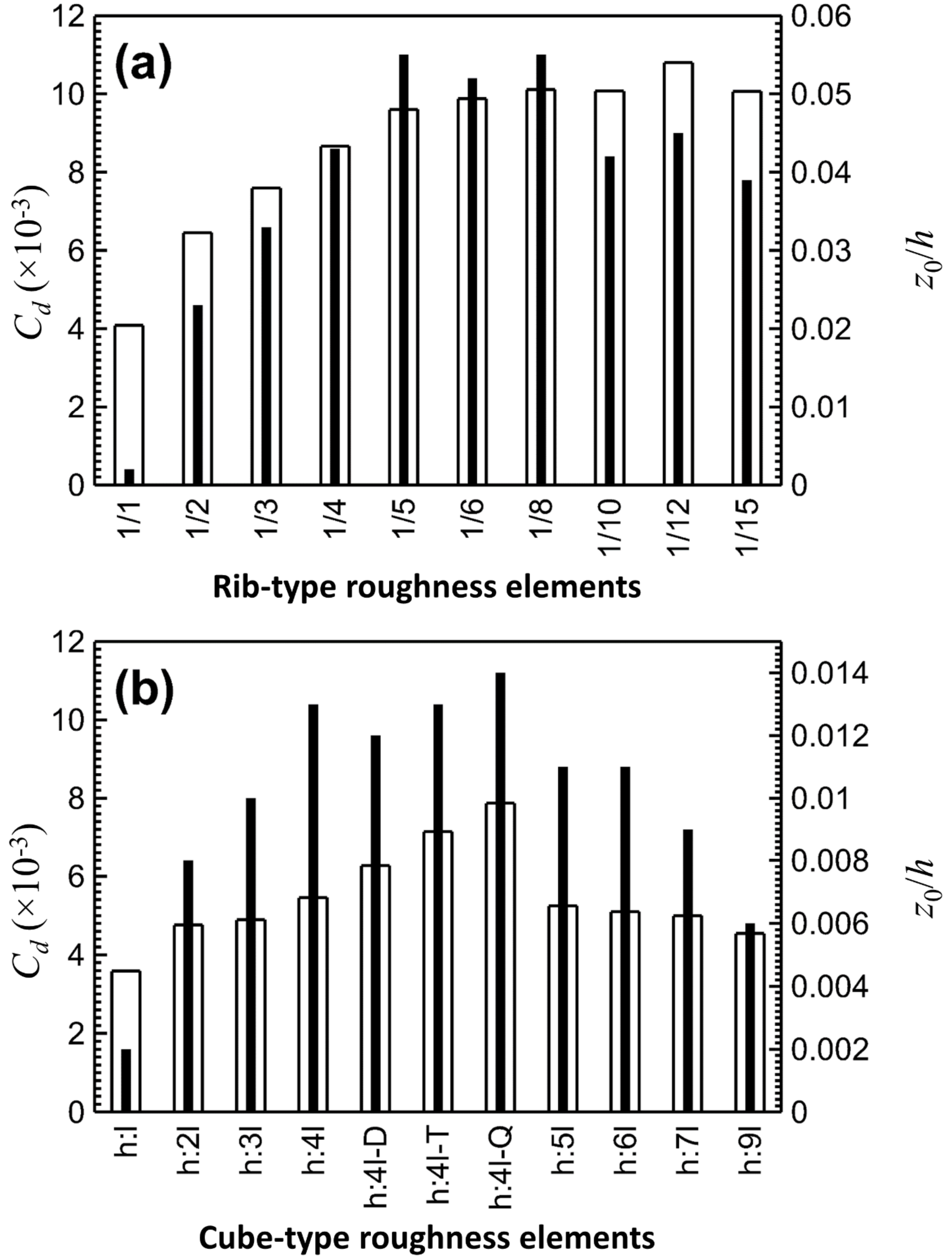

Figure 2. Comparison of the drag coefficient C_d (empty bars) and the dimensionless roughness length scale z_0/h (filled bars) over (a) rib- and (b) cube-type roughness elements. Here, h is the size of the roughness elements.

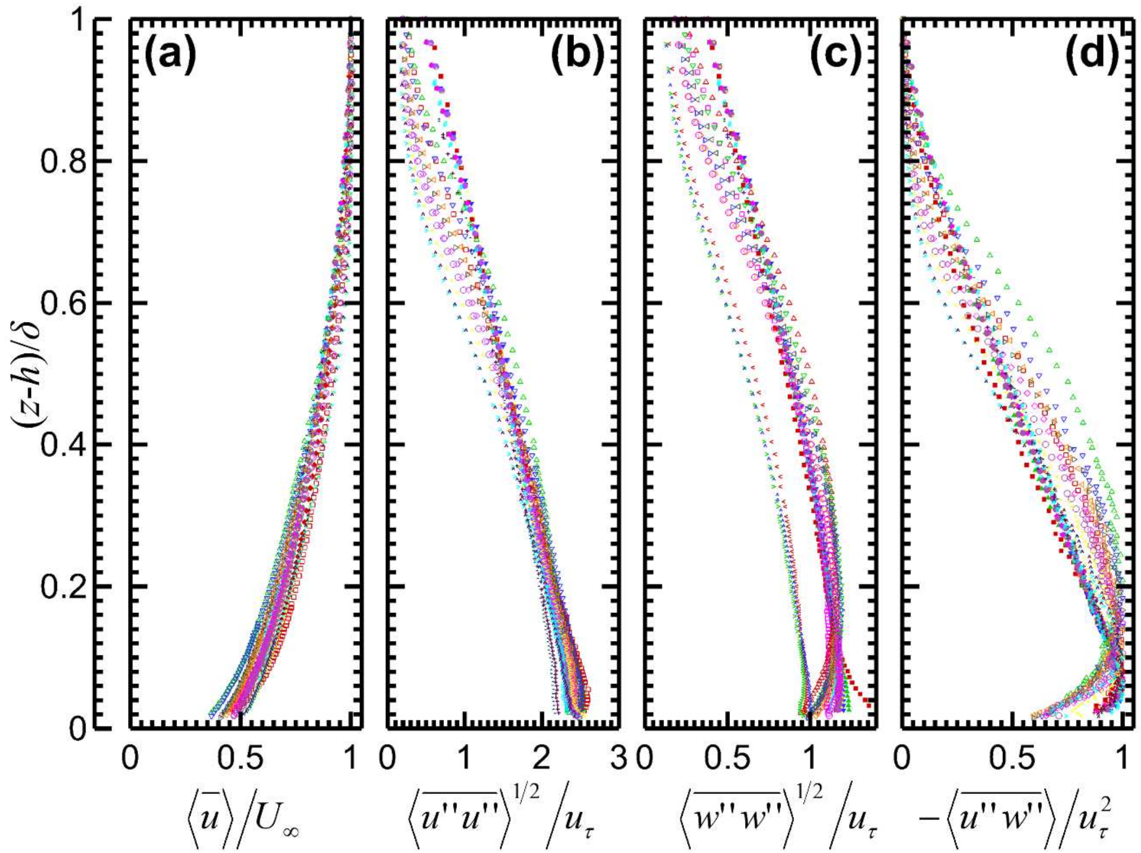

Figure 3. Dimensionless vertical profiles of flow properties over rib- and cube-type roughness elements expressed as functions of wall-normal distance $(z\text{-}h)/\delta$. (a) Mean wind speed $\langle\bar{u}\rangle/U_\infty$; (b) streamwise fluctuating velocity $\langle\overline{u''u''}\rangle^{1/2}/u_\tau$; (c) vertical fluctuating velocity $\langle\overline{w''w''}\rangle^{1/2}/u_\tau$ and (d) momentum flux $\langle u''w''\rangle/u_\tau^2$. AR = 1/1 (□); 1/2 (△); 1/3 (▽); 1/4 (▷); 1/5 (◁); 1/6 (◇); 1/8 (○); 1/10 (<); 1/12 (>); and 1/15 (^). LEGO *h*:*l* (■); *h*:2*l* (▲); *h*:3*l* (▼); *h*:4*l* (▶); *h*:5*l* (◀); *h*:6*l* (◆); *h*:7*l* (●); *h*:9*l* (*); *h*:4*l*-D (#) *h*:4*l*-T (+); and *h*:4*l*-Q (-).

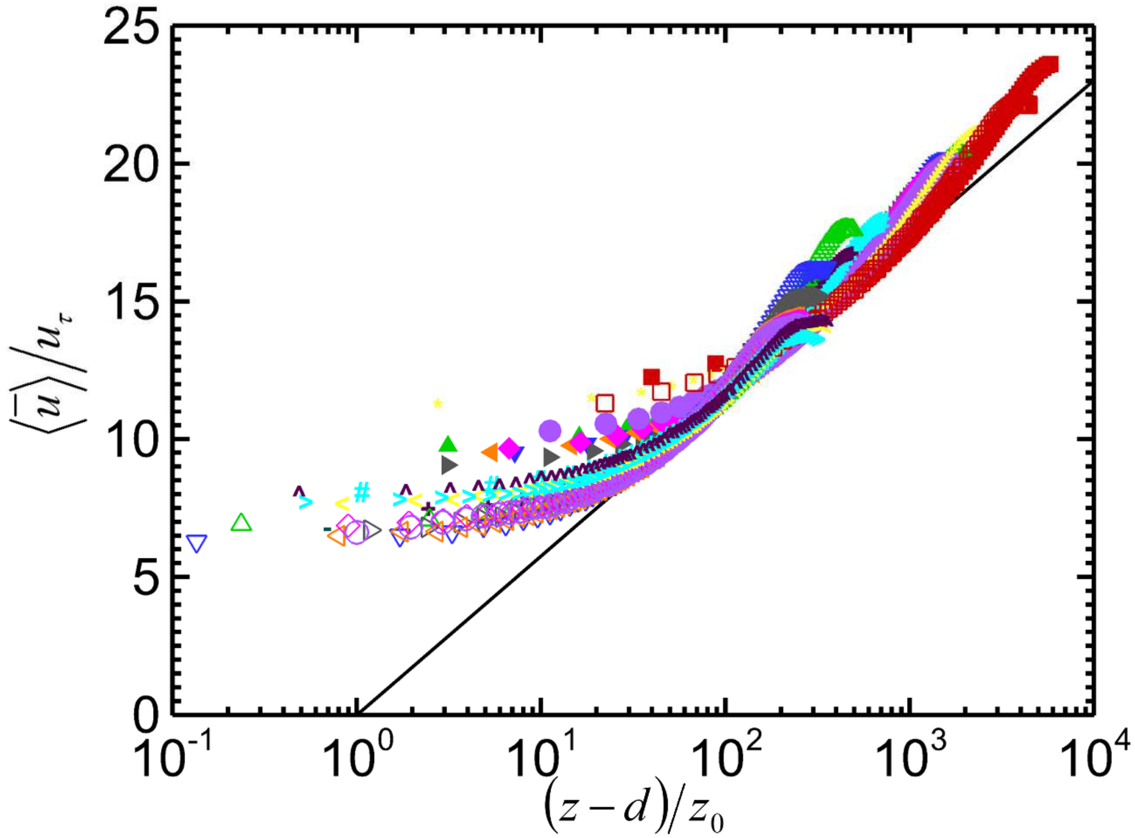

Figure 4. Dimensionless mean wind speed $\langle \bar{u} \rangle / u_\tau$ over rib- and cube-type roughness elements plotted against dimensionless wall-normal distance $(z - d)/z_0$ in semi-logarithmic scale. AR = 1/1 (□); 1/2 (△); 1/3 (▽); 1/4 (▷); 1/5 (◁); 1/6 (◇); 1/8 (○); 1/10 (<); 1/12 (>); and 1/15 (^). LEGO® *h*:*l* (■); *h*:2*l* (▲); *h*:3*l* (▼); *h*:4*l* (▶); *h*:5*l* (◀); *h*:6*l* (◆); *h*:7*l* (●); *h*:9*l* (*); *h*:4*l*-D (#) *h*:4*l*-T (+); and *h*:4*l*-Q (-). Also shown is the conventional logarithmic law of the wall (solid dark line).

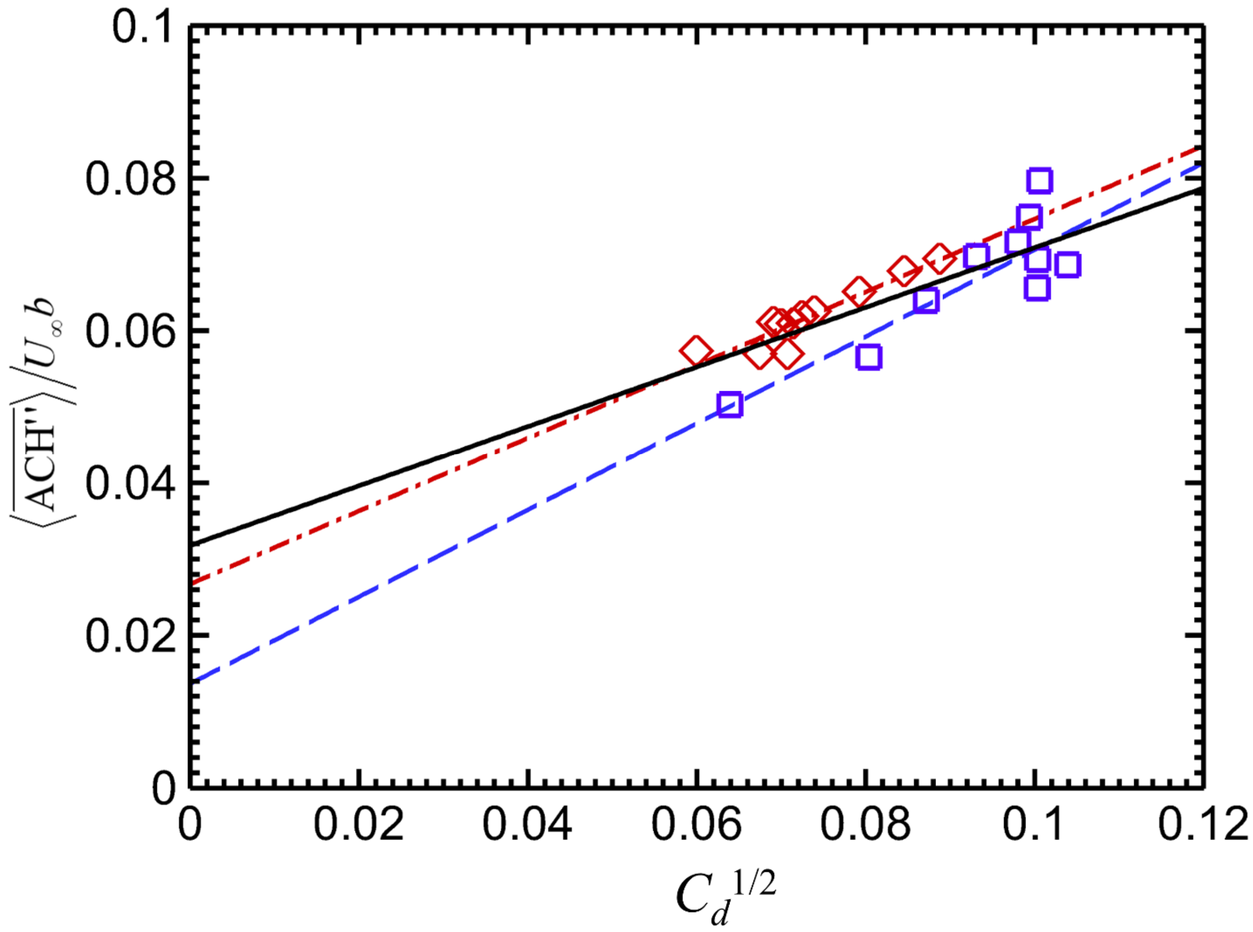

Figure 5. Dimensionless turbulent air exchange rate $\langle \overline{\mathrm{ACH''}} \rangle / U_\infty b$ plotted against root of drag coefficient $C_d^{1/2}$ over different surface roughness configurations. Rib- (□) and cube-type (◇) roughness elements. Also shown are the linear regression for rib-type data points (*blue dashed line*; R^2= 0.75), for cube-type data points (*red dashed line*; R^2= 0.86) and for all the data points (*dark solid line*; R^2= 0.68).

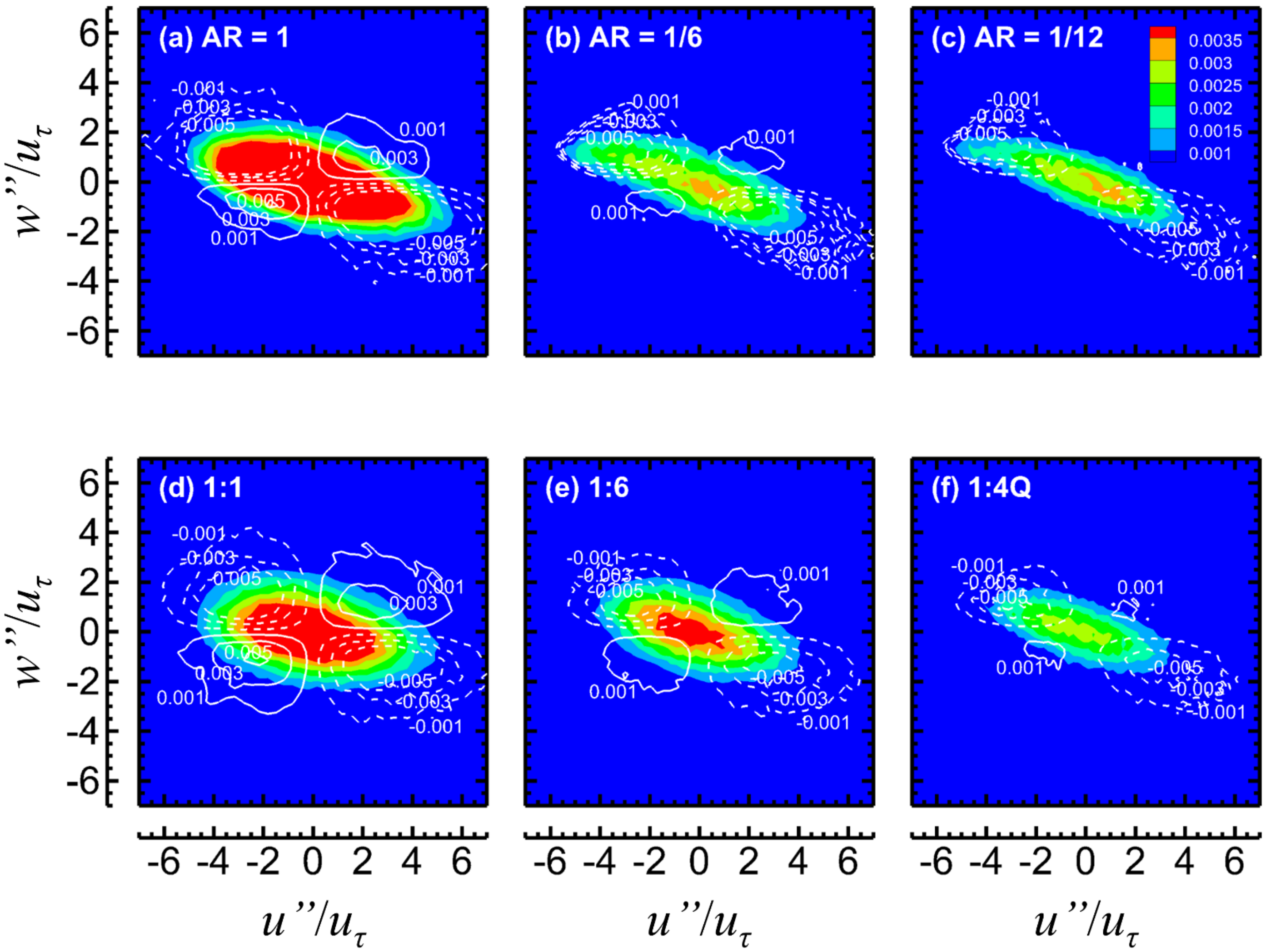

Figure 6. Shaded contours of joint probability density function (JPDF) $P(u'', w'')$ and contour lines of covariance integrand $u''w''P(u'', w'')$ at roof level over street canyons of hypothetical urban areas of (a) AR=1/1; (b) AR=1/6; (c) AR=1/12; (d) h:l; (e) h:6l and (f) h:4l-Q.

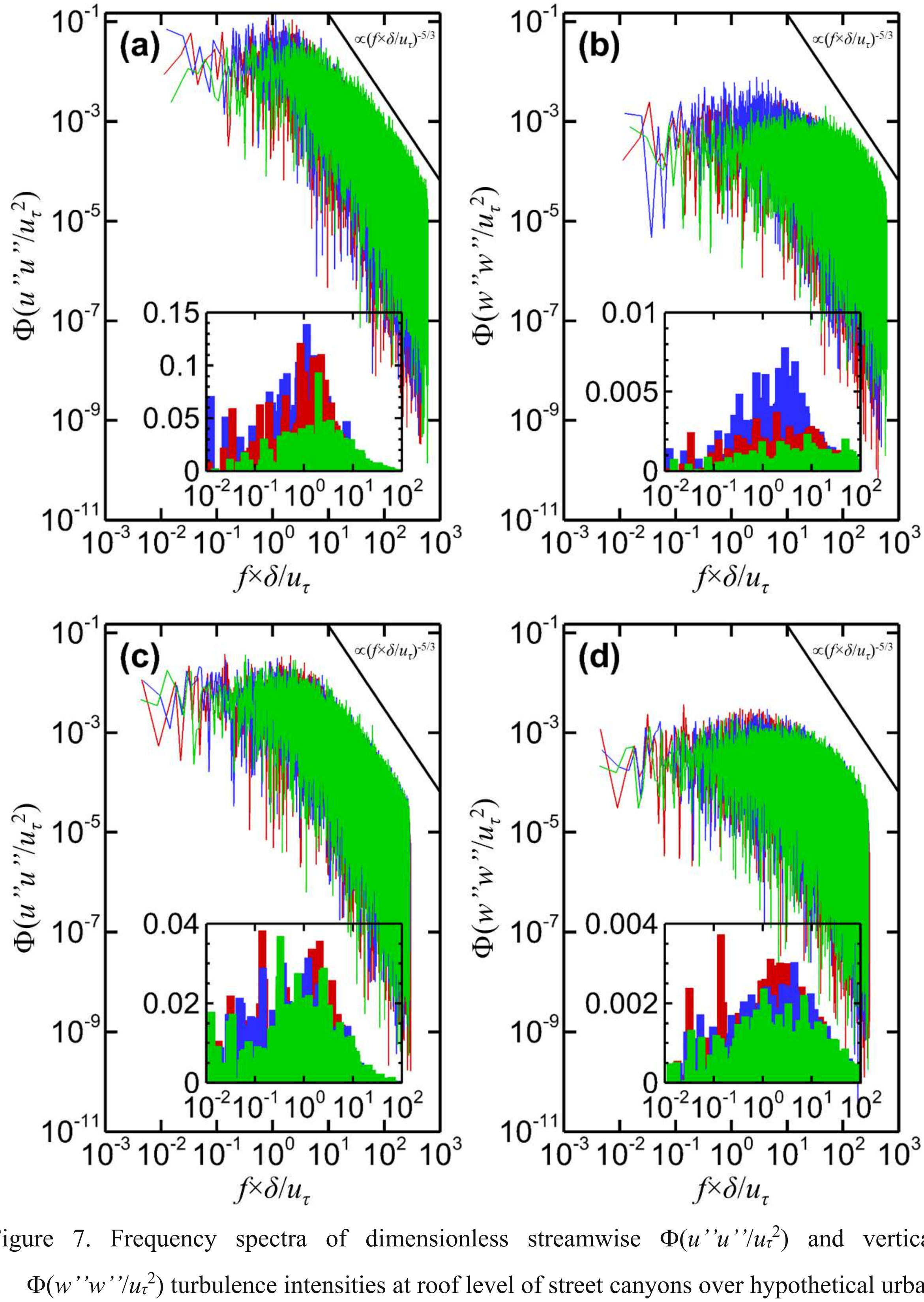

Figure 7. Frequency spectra of dimensionless streamwise $\Phi(u''u''/u_\tau^2)$ and vertical $\Phi(w''w''/u_\tau^2)$ turbulence intensities at roof level of street canyons over hypothetical urban areas. (a) and (b) are rib-type roughness elements for AR=1 (green), AR=1/6 (blue) and AR=1/12 (red). (c) and (d) are cube-type roughness elements for *h*:*l* (green), *h*:6*l* (blue) and *h*:4*l*-Q (red). Inserted figures express the *y* axes in linear scales for clarity.